Volume 2
Number 5
September 2025
Pages 619–774

RSC Mechanochemistry

rsc.li/RSCMechanochem

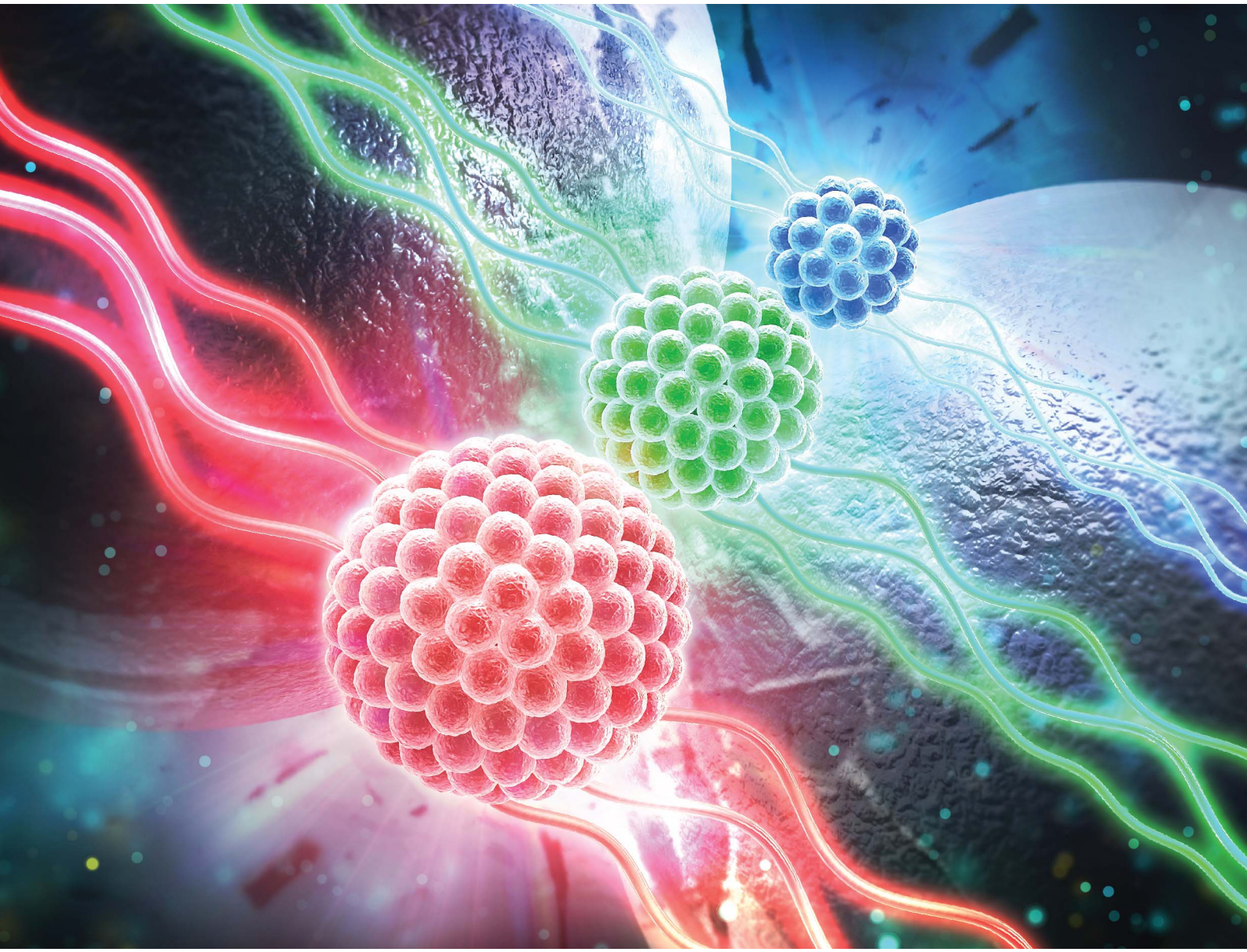

ISSN 2976-8683

ROYAL SOCIETY OF CHEMISTRY

PAPER
Takashi Shirai *et al.*
Photoluminescence evolution of functional silicon quantum dots assembled *via* a sustainable mechanochemical process

RSC Mechanochemistry

ROYAL SOCIETY OF CHEMISTRY

PAPER

View Article Online
View Journal | View Issue

Cite this: *RSC Mechanochem.*, 2025, **2**, 641

Photoluminescence evolution of functional silicon quantum dots assembled *via* a sustainable mechanochemical process†

Yuping Xu, [a] Yunzi Xin [a] and Takashi Shirai *[ab]

In the present work, we report a sustainable, room-temperature mechanochemical approach for synthesizing functional silicon quantum dots (Si QDs) with tunable photoluminescence (PL) in the visible range. Using hydrogen silsesquioxane as a precursor, precise control over the size and surface chemical state of Si QDs is achieved through controlled ball-milling and subsequent chemical etching and hydrosilylation. Discrete element method simulations reveal that the cumulative supra-critical impact energy (E_{sup}), defined as the total impact energy exceeding a critical threshold (e_{crit}) required for chemical activation, plays a dominant role in driving the formation of Si radicals and Si–H bond cleavage, which are key steps in crystallite growth. Under high-energy milling conditions using larger balls, a significant portion of collisions exceed e_{crit}, thereby enhancing the efficiency of solid-state chemical reactions and leading to the formation of larger Si QDs. The PL red shift observed across blue-, green-, and red-emitting Si QDs is attributed to a size–surface coupling mechanism. For smaller Si QDs, PL originates from quantum-confined band-edge transitions and shallow surface states, enabled by high alkyl chain coverage. Larger Si QDs exhibit red-shifted, excitation-independent emission dominated by deep oxide-related surface states, stemming from enhanced oxidation and reduced organic passivation. These findings highlight the interplay between mechanical energy input, structural/size evolution, and surface chemistry in tailoring the optical properties of Si QDs.

Received 24th April 2025
Accepted 2nd July 2025

DOI: 10.1039/d5mr00054h

rsc.li/RSCMechanochem

Introduction

Colloidal semiconductor quantum dots (QDs) exhibiting tunable emission wavelengths, distinct exciton absorption peaks, remarkable photostability, and solution processability in device fabrication have a wide range of important and emerging applications in the fields of optoelectronics, optics, photonics, and bioengineering.[1,2] Diamond cubic crystalline silicon (Si) QDs have garnered significant attention as promising next-generation functional materials, stemming from their natural abundance, non-toxicity, excellent biocompatibility, and unique optical properties.[3] Affecting the efficient emission and absorption of light, silicon in the bulk state is a semiconductor with an indirect bandgap. Nowadays, a decrease in particle size to <5 nm (the excitonic Bohr radius of Si) allows the conversion of Si particles from indirect to direct bandgap materials with a high quantum yield (QY) of photoluminescence (PL) of up to 90%.[4,5] The quantum confinement effect increases the band gap of Si as the size of the quantum structure decreases, which results in a blue shift in optical luminescence and energy absorption.[6,7] The optical and electrical properties of Si QDs in general are also extremely sensitive to and tunable by surface chemistry.[8,9] Efficient optical absorption/emission and spectral tunability are fundamental prerequisites for advancing various applications in photonics, optoelectronics, and materials science. Nowadays, for producing nanosized Si particles, various methods are well-studied and can be divided into top-down and bottom-up approaches.[10] The representative conventional approaches for synthesizing Si QDs with wavelength-tunable PL are summarized in Table 1 and can be stated as two main routes. One is precise size tuning *via* an etching process followed by the synthesis of Si particles or direct etching of Si sources, in which the sizes do not correspond to the photoluminescent region.[11–15] Etching of Si particles is a common process used to modify their size, shape, and surface properties. However, it is well known that the etching process makes the surface more susceptible to oxidation or degradation when exposed to air or other environmental factors. Moreover, etching time and conditions should be carefully controlled to achieve the desired properties, making it a critical process. Most importantly, etching processes may involve the use of hazardous chemicals or produce waste by-products that require proper disposal and handling. Another route is direct size or surface control synthesis from precursors without further size

[a]*Advanced Ceramics Research Center, Nagoya Institute of Technology, Gokiso-cho, Showa-ku, Nagoya, Aichi 466-8555, Japan. E-mail: shirai@nitech.ac.jp*

[b]*Program of Advanced Ceramics, Department of Engineering, Graduate School of Engineering, Nagoya Institute of Technology, Gokiso-cho, Showa-ku, Nagoya, Aichi 466-8555, Japan*

† Electronic supplementary information (ESI) available: Table S1, Fig. S1 and S2, and movies (.avi) showing representative simulated ball motion behaviours during the milling process of A1–A4. See DOI: https://doi.org/10.1039/d5mr00054h

tuning processes.[10,16–20] Si QDs with tunable PL across the visible and near-infrared (NIR) spectra have been prepared through thermal pyrolysis (1100–1400 °C) of hydrogen silsesquioxane ($(HSiO_{1.5})_n$, $n > 8$ or $H_8Si_8O_{12}$) polymers[19–23] and thermal decomposition (140–500 °C) of alkylsilanes[16–18] at well-defined temperature and time. Surface passivated Si QDs with PL extended to encompass the full color spectrum within the 400–800 nm wavelength range *via* surface engineering with alkyl, amine, phosphine, and acetal functional groups as well as halide ligands have been reported.[9,20,24–27] However, for these methods, high temperature and precise manipulation of temperature/time are critical conditions and significant drawbacks.

Functional Si QDs synthesized *via* a green and sustainable room-temperature mechanochemical route from the $(HSiO_{1.5})_n$ polymer have been first developed by our group.[28] This facile mechanochemical route opens a new avenue for the smart synthesis of functional nanomaterials. In the present work, we further investigate the synthesis of functional Si QDs exhibiting tunable PL across the visible spectrum *via* a green and sustainable room-temperature mechanochemical approach. Through controlled mechanochemical treatment followed by a hydrosilylation process, both the size and surface chemical state of the Si QDs are precisely tailored. This study demonstrates the successful fabrication of Si QDs emitting red, green, and blue PL by employing a more refined strategy that adjusts the ratio of large and small milling balls. Furthermore, by integrating discrete element method (DEM) simulations, we unravel the correlation between ball-milling impact energy profiles and structural evolution. Through modulation of mechanical energy input *via* controlled milling parameters, the size and crystallinity of the Si QDs are selectively engineered. DEM analysis reveals that high-energy collisions dominate crystallite growth by mediating Si–H bond cleavage and radical-initiated reconstruction. Moreover, spectral characterization demonstrates that the red shift in PL from blue to red emission cannot be solely attributed to quantum size effects. Instead, the tunable PL can be attributed to several interdependent factors: (i) size-dependent quantum confinement, (ii) surface ligand coverage modulating radiative recombination efficiency, and (iii) oxygen passivation suppressing non-radiative pathways in larger QDs. This mechanism underscores the necessity of holistic control over both nanoscale crystallinity and atomic-scale surface states in the design of functional Si QDs. Unlike conventional thermal or etching-based approaches, this ambient-condition method avoids harsh experimental conditions such as elevated temperatures and prolonged reaction times, and it minimizes the use of hazardous chemicals (as described in Table 1). This provides a safer, energy-efficient, and scalable alternative that aligns with sustainable development goals.

Table 1 Comparison between conventional synthetic approaches of Si QDs with wavelength-tunable PL and the proposed method

Synthesis conditions	Surface groups	Wavelength range or color of PL	Hydrophobicity	Ref.
Plasma irradiation of SiH_4 → HF/HNO_3/MeOH etching (10–20 min) → hydrosilylation	Phosphorus-doped/dodecyl-	467–746 nm as etching proceeded	√	11
Plasma irradiation of SiH_4 → HF/HNO_3/MeOH etching → hydrosilylation	H-/pentene/hexene/octene/dodecane	Red, yellow, and green as etching proceeded	√	12
SiO_x → HF/HNO_3 etching (0.5–18 min)	Propionic acid	Yellow, green, and blue as etching proceeded	—	13
SiH_4 plasma → CF_4/H_2 plasma etching	C-/F-	441–740 nm as plasma etching proceeded	—	14
Electrochemical etching → H_2O_2/EtOH oxidation, 0.5–24 h	SiO_xH_y shell	460–665 nm as etching proceeded	—	15
Ar-SiH_4 plasma, 1.4 Torr, 200 W	—	700–810 nm as plasma proceeded	—	16
Thermal degradation of diphenylsilane in octanol, 500 °C, 140–345 bar	Alkyl-	Blue, blue-green	√	17
Thermal decomposition of chloroalkylsilane, 140 °C, 6–72 h	Octadecylamine	430–600 nm as heating proceeded	√	18
Thermal pyrolysis (>1000 °C) of the $(HSiO_{1.5})_n$ polymer ($n \geq 8$) → HF acid etching → surface passivation	H-/alkyl-/amine, phosphine/acetal/halide…	400–800 nm, depending on thermal temperature/time, acid etching time, passivation groups…	√	9, 10, 19 and 20
Room temperature mechanochemical treatment of the $(HSiO_{1.5})_n$ polymer ($n > 8$) → HF acid etching → surface passivation	Alkyl-	Red, green, and blue as the ball size during mechanochemical treatment	√	*Present work*

Experimental

Materials

Trichlorosilane ($HSiCl_3$, >98%) was purchased from Tokyo Chemical Industry Co., Ltd (Tokyo, Japan) and stored in a refrigerator prior to use. Hexane (96%, guaranteed grade), methanol (95%, guaranteed grade), ethanol (95%, guaranteed grade), hydrofluoric acid (HF, 49%, mass/mass, guaranteed

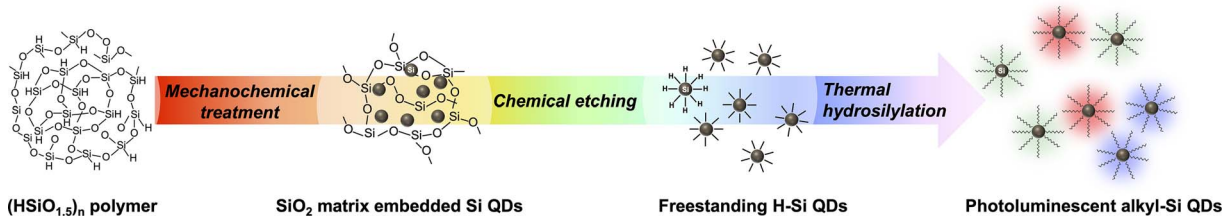

Scheme 1 Synthesis procedure of photoluminescent Si QDs from the $(HSiO_{1.5})_n$ polymer.

grade), hydrochloric acid (HCl, 35–37%, mass/mass, guaranteed grade), and 1-decene (95%, first grade) were purchased from FUJIFILM Wako Pure Chemical Corp. Acetone of ACS grade was obtained from Kanto Chemical Corp. All chemicals were used as received without further purification.

Mechanochemical treatment of the $(HSiO_{1.5})_n$ polymer

1 g of lab-synthesized $(HSiO_{1.5})_n$ polymer[28] from $HSiCl_3$ was transferred into an 80 ml zirconia (ZrO_2) milling vessel containing a total of 40 g of ZrO_2 balls with varied diameters (5 mm and 10 mm). The loading was conducted inside an Ar-filled glovebox. The vessel was sealed and subjected to mechanochemical treatment using a high-energy planetary ball mill (Pulverisette 7 Premium Line, Fritsch) at 400 rpm for 3 h at ambient temperature (~25 °C). The resulting samples were labelled as follows: A1 (101 balls with a diameter of 5 mm), A2 (a mixture of 69 balls with a diameter of 5 mm and 4 balls with a diameter of 10 mm), A3 (a mixture of 45 balls with a diameter

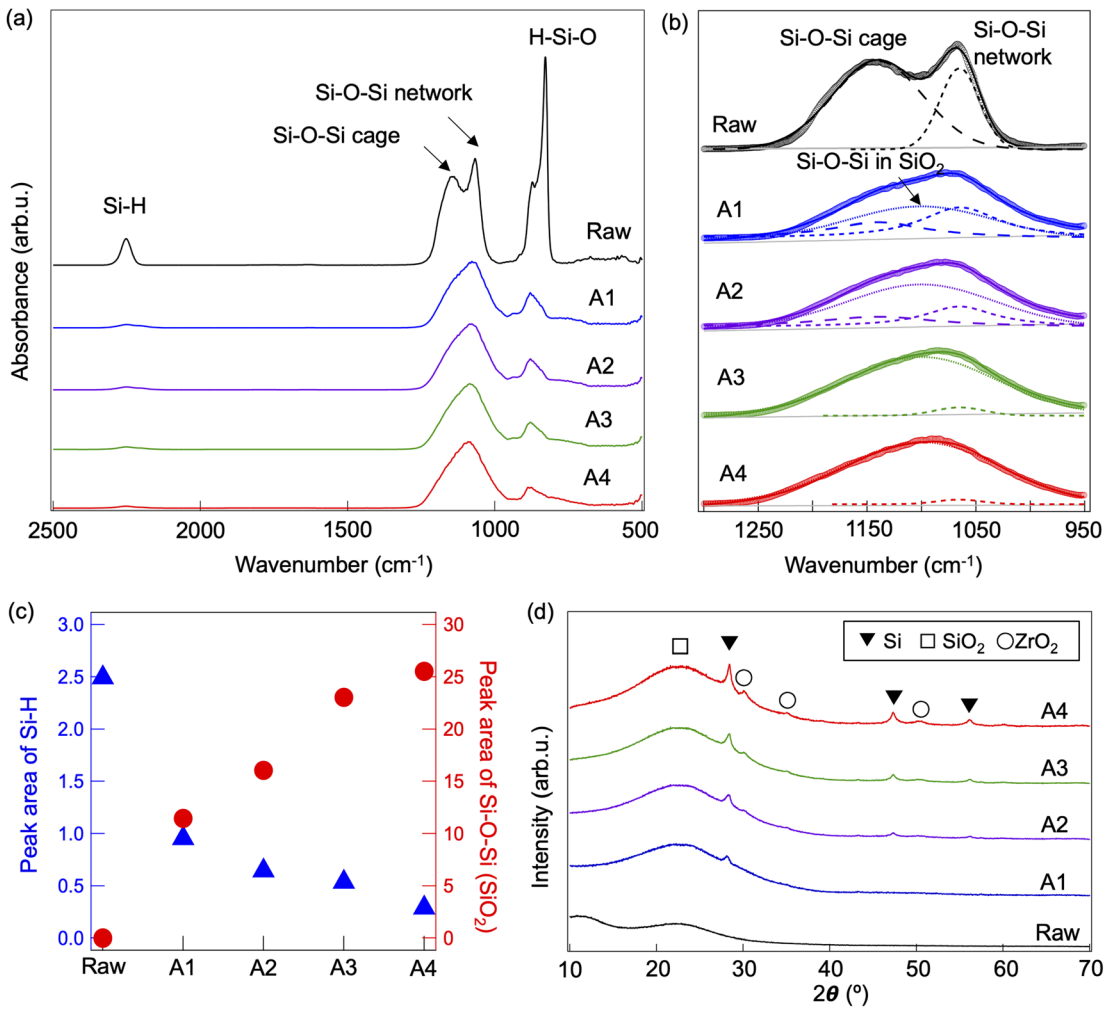

Fig. 1 (a) FT/IR spectra of the $(HSiO_{1.5})_n$ polymers before and after the planetary high energy ball milling process. (b) Fitted FT/IR peaks of Si–O–Si in the region of 1300–950 cm^{-1}. (c) The integrated peak areas of the bands corresponding to the Si–H (left axis) and Si–O–Si bending modes (right axis) calculated from the FT/IR spectra for the altered mixed balls. (d) PXRD patterns of the raw and mechanochemically treated $(HSiO_{1.5})_n$ polymers.

of 5 mm and 7 balls with a diameter of 10 mm), and A4 (13 balls with a diameter of 10 mm).

Liberation and surface functionalization of Si QDs

The surface passivated Si QDs were synthesized as reported in our previous work.[28] Briefly, after mechanochemical treatment, the resulting $(HSiO_{1.5})_n$ polymers consisted of a SiO_2-like matrix surrounding Si QDs. To extract free-standing hydrogen-terminated Si QDs (H-Si QDs) from the mechanochemically treated composite, 100 mg of the treated polymer (A1, A3, and A4) was mixed with 1.5 ml of ethanol, 150 μl of 25% HCl, and 6 ml of 49% HF in a Teflon vessel. The reaction was conducted in the dark for 6 h. *Caution: HF is corrosive and highly toxic and must be handled with proper protective equipment and in accordance with institutional safety regulations*. The resulting H-Si QDs were extracted into toluene and purified by centrifugation at 15 000 rpm for 30 min to remove the organic supernatant. For surface passivation, the H-Si QDs were dispersed in 10 ml of 1-decene and refluxed under an Ar atmosphere at 150 °C for 12 h to perform thermal hydrosilylation. The reaction mixture was then treated with an ethanol/methanol mixture (3 : 1 v/v, 20 ml) and centrifuged (15 000 rpm, 20 min) to remove excess 1-decene. The alkyl-passivated Si QDs (alkyl-Si QDs) were further purified by repeated precipitation three times using a methanol/toluene mixture (3 : 1 v/v) and redispersed in toluene. The final suspension was filtered through a PTFE membrane (pore size: 200 nm) and stored for subsequent characterization.

Characterization

The structural evolution of the $(HSiO_{1.5})_n$ polymer before and after milling was analyzed by FTIR spectroscopy (FT/IR; FT/IR-V6000, JASCO Corp.) using the diffuse reflectance method. Powder X-ray diffraction (PXRD; Ultima IV, Rigaku Corp.) with Cu Kα radiation (40 kV, 40 mA) was employed to confirm the crystallinity of the Si QDs. High-resolution transmission electron microscopy (HR-TEM; JEM-ARM200F, JEOL Ltd) was used to observe the morphology and lattice structure, with samples prepared by drop-casting onto carbon-coated copper grids. X-ray photoelectron spectroscopy (XPS; M-probe SSX-100, S.S.I., USA) with Al Kα X-ray (hn 1/4 1486.6 eV) radiation was used to examine the chemical state. PL spectra were recorded using a fluorescence spectrometer (FP-8500, JASCO Corp.). The absolute photoluminescence quantum yield (PLQY) was determined with a PLQY spectrometer (C13534, Hamamatsu Photonics K.K.). Dynamic light scattering (DLS; Zetasizer, Malvern Panalytical Ltd) was used to evaluate the hydrodynamic size distribution of the Si QDs in toluene. PL lifetime measurements were performed using a time-resolved spectroscopy system (TSP-2000 M, UNISOKU Co., Ltd).

Results and discussion

Scheme 1 illustrates the synthesis process presented in this study to convert the $(HSiO_{1.5})_n$ polymer into functional Si QDs with tunable PL. The process consists of three main steps: (1) the $(HSiO_{1.5})_n$ polymer was subjected to mechanochemical treatment with precisely controlled ball size; (2) the resulting SiO_2 matrix embedded Si QDs were chemically etched to obtain H-Si QDs; and (3) the H-Si QDs were thermally hydrosilylated with 1-decene to produce decyl-passivated Si QDs exhibiting visible light emission under UV light. To gain insight into the structural evolution during the mechanochemical process, FT/IR spectroscopy was employed to analyse both the raw and mechanochemically treated polymers. As shown in Fig. 1a, it is confirmed that the raw $(HSiO_{1.5})_n$ polymer comprises both cage and network structures with the appearance of a band of Si–O–Si stretching mode at approximately 1100 cm^{-1}, which can be divided into two sub-bands: at 1140 cm^{-1} and 1065 cm^{-1}, owing to the cage and network-structured Si–O–Si at different angles, respectively. In addition, Si–H stretching mode at 2252 cm^{-1} and H–Si–O stretching mode at 830 cm^{-1} are also confirmed, consistent with previously reported FT/IR spectra of the $(HSiO_{1.5})_n$ polymers.[21,22] Compared to the raw $(HSiO_{1.5})_n$ polymer, a significant change in the chemical structure occurs after mechanochemical treatment, especially for relatively larger ball cases, since the peak intensity and shape of the Si–H stretching band, Si–O–Si bands, and H–Si–O are obviously altered. Meanwhile, a new and broad featureless absorption centred at *ca.* 1100 cm^{-1} that could be assigned to Si–O–Si bending in a SiO_2-like network appears.[29] As shown by further analysis in Fig. 1b and c, a clear decrease in the peak intensity of Si–H stretching

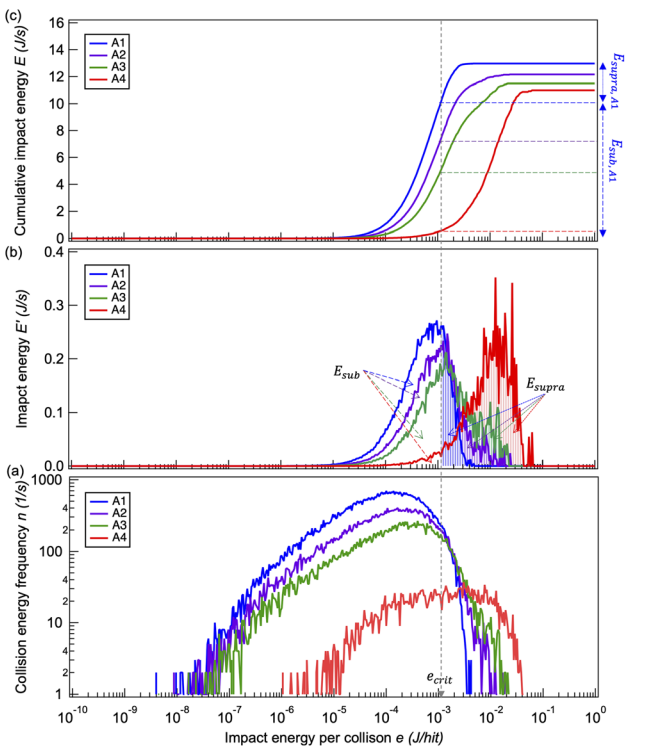

Fig. 2 (a) Distribution of collision frequency n that occurred at a certain impact energy value e under various conditions of A1, A2, A3, and A4. ($e_{crit} = 1.1 \times 10^{-3}$ J per hit). (b) Impact energy E' imparted to the system by collisions within a certain impact energy value e. The integrated area to the left of e_{crit} represents E_{sub} and the integrated area to the right of e_{crit} represents E_{supra}. (c) Cumulative impact energy E.

with increased Si–O–Si bending was observed upon increasing larger milling balls, which can supply higher impact energy in the present mechanochemical system according to our previous calculation.[28] These results suggest that the network structure in $(HSiO_{1.5})_n$ polymer molecules collapses, and a new SiO_2-like network redistributes with a loss of Si–H bonds by inducing efficient impact energy. Fig. 1d displays the PXRD patterns of raw and mechanochemically treated $(HSiO_{1.5})_n$ polymers. Compared to the broad diffraction peak that arises from the amorphous SiO_2-like matrix of raw $(HSiO_{1.5})_n$ polymer, when it is mechanochemically processed by balls with a diameter of 5 mm, a weak diffraction peak corresponding to the (111) reflection of the diamond lattice Si appears,[19,21] indicating the formation of an inferior or short-range crystalline order of Si. Peaks from (220) and (311) crystal planes of diamond structured Si appear,[19,21] and these three peaks notably increase in intensity with relatively larger milling balls with a diameter of 10 mm, indicating increased crystallinity of oxide-embedded Si. These results indicate oxide-embedded high-range crystalline Si order growth with the collapse of the silsesquioxane structure by providing high impact energy through efficient planetary ball-milling with larger balls (10 mm) in the present work.

Moreover, the effect of impact energy was further examined through simulations using KIK DEM software (ver. 1.4), which modelled a system consisting solely of balls in the ball mill. The detailed parameter information of the simulation is presented in Table S1 (ESI†). The representative ball motion behaviours during milling of A1–A4 are displayed in movies (ESI†). The motion of a spherical particle i (with radius r) is governed by the forces exerted by the k_i particles in contact with it. The equations of motion describing translation and rotation are as follows:[30–32]

$$m_i \frac{dv_i}{dt} = \sum_{j=1}^{k_i} \left(F_{ij}^{n} + F_{ij}^{t} \right) + m_i g \quad (1)$$

$$I_j \frac{d\omega_i}{dt} = \sum_{j=1}^{k_i} \left(r_i F_{ij}^{t} \right) + R_r \quad (2)$$

where m denotes the mass of a ball, t is the time, v is the translational velocity, and k is the number of particles. F^n and F^t represent the normal and tangential contact forces, respectively. The gravitational acceleration is denoted by g, I is the moment of inertia, ω is the rotational velocity, and R_r represents the rolling resistance, which accounts for rolling friction between particles in the rotational direction. The subscript ij indicates that the force is acting between particle i and particle j.

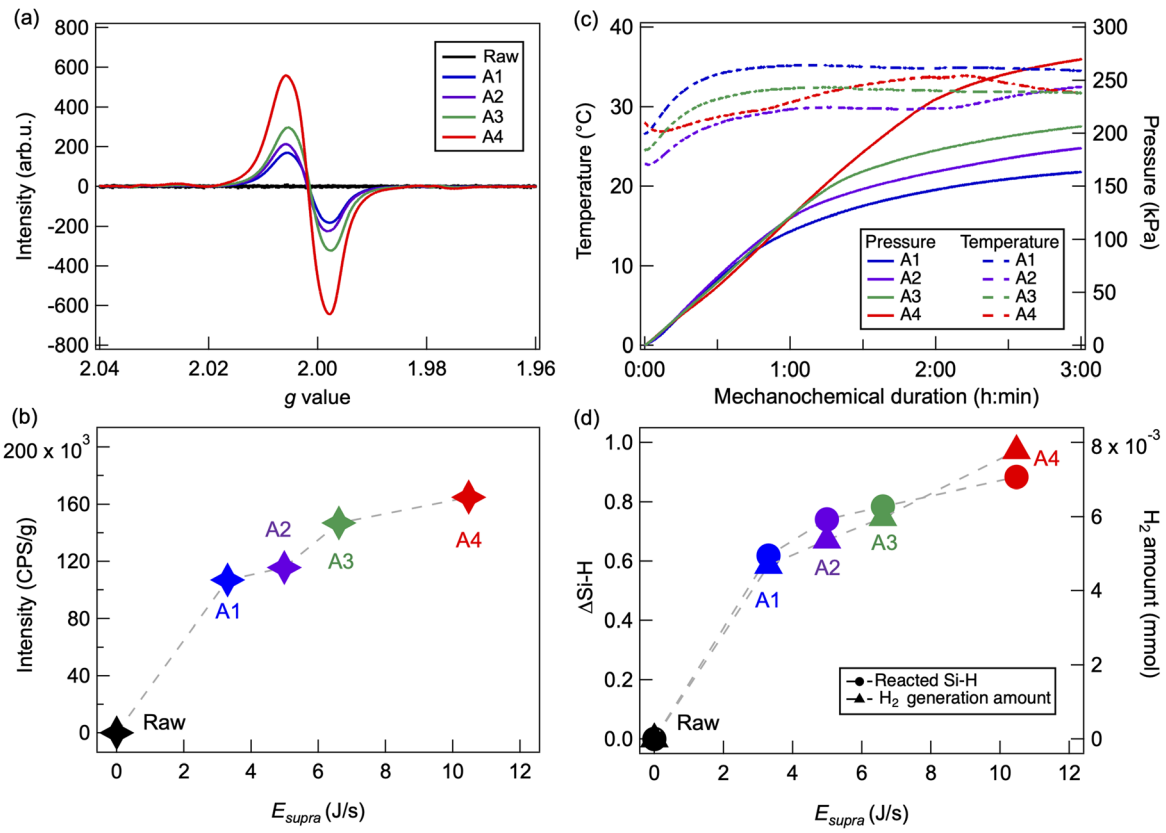

Fig. 3 (a) ESR spectra of the raw and mechanochemically treated $(HSiO_{1.5})_n$ polymers under conditions of A1, A2, A3, and A4. (b) Quantification of radical intensity normalized by sample mass as a function of E_{supra} under conditions of A1, A2, A3 ,and A4. (c) *In situ* temperature (left axis, dashed line) and pressure (right axis, solid line) monitored in the planetary ball-milling vessel during the mechanochemical treatment of the $(HSiO_{1.5})_n$ polymer under conditions of A1, A2, A3, and A4. (d) Correlation between the reduction of the Si–H bond evaluated from FT-IR (left axis), the generated H_2 amount calculated according to the *in situ* temperature and pressure (right axis) and E_{supra}.

The cumulative impact energy (cumulative value, E) is calculated using eqn (3) as follows:

$$E = \sum_{j=1}^{n} \left(\frac{1}{2t_s} m {v_{Rj}}^2 \right) \quad (3)$$

Here, the kinetic energy of the colliding ball from the perspective of one ball (calculated using relative velocity) is considered as the energy of one collision. The simulations were performed for 5 seconds from the start of rotation of the container, but the cumulative impact energy calculation was performed for 1 second from 4 seconds to 5 seconds later. At this point, it was confirmed that the motion of the balls was steady and there was almost no fluctuation with time. Here, v_R is the relative velocity between the balls, t_s is the time for which the impact energy is calculated in the simulation (here, 1 second), and n is the frequency, the number of collisions of the balls during the time for which the calculation is performed. In this study, we also calculated the distribution of the number of collisions corresponding to a certain energy from the calculated data of the energy of each collision (eqn (4)).

$$e_j = \frac{1}{2} m {v_{Rj}}^2 \quad (4)$$

For milling A1–A4, the effect of the ball diameter on the impact energy distribution is shown as Fig. 2a–c. Fig. 2a illustrates the distribution of collision frequency that occurred at a certain impact energy value. Fig. 2b shows the impact energy-weighted distribution, reflecting the impact energy (E') imparted to the system by collisions within a certain impact energy value. It can be estimated by multiplying the impact energy of individual collisions by their frequency. Fig. 2c implies the cumulative impact energy, E, obtained by integrating the curve in Fig. 2b. When the ball diameter is changed, a considerable difference appears in the region, in which the impact energy is distributed. As shown in Fig. 2a, when the total mass of the balls remains unchanged, the larger the balls used, the fewer the number of collisions, but the collisions are distributed in a higher energy region. Conversely, the energy is distributed in a low region when the ball diameter is small, but the number of collisions is significantly larger. In mechanochemical

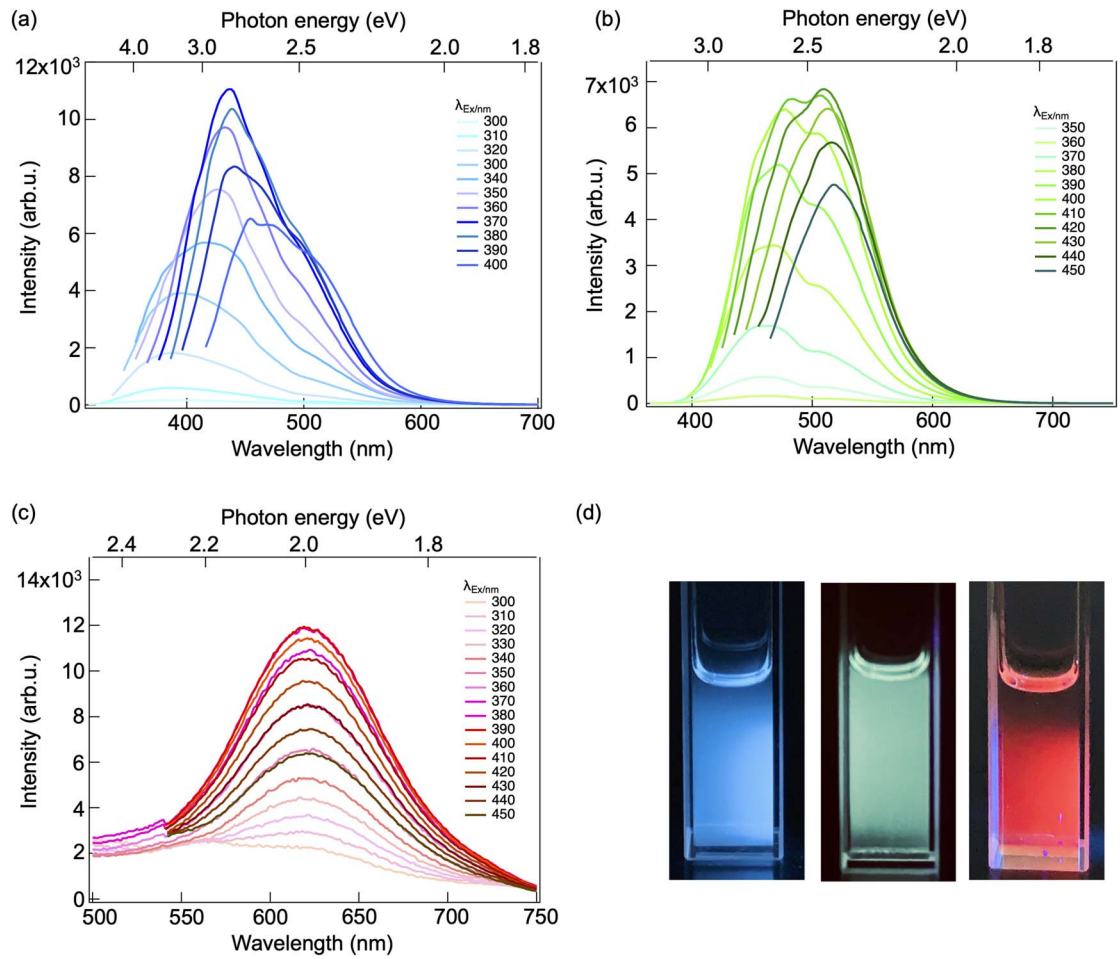

Fig. 4 PL spectra of alkyl-Si QDs recorded by changing the excitation wavelength obtained from (a) A1, (b) A3, and (c) A4. (d) Photography of alkyl-Si QDs dispersed in toluene under UV375 light (from left to right: A1, A3, and A4) emitting in blue-, green- and, red-light regions, respectively.

processes, a chemical reaction is initiated when the impact energy transferred during a single collision exceeds a certain threshold. Here, we define this threshold as the critical impact energy (e_{crit}, J per hit), which corresponds to the minimum impact energy required to overcome the activation barrier for chemical reactions. In our previous study, it was experimentally observed that when 3 mm milling balls were used, no significant chemical reactions were detected: no crystalline Si formation was observed, and no measurable H_2 evolution occurred.[28] Based on this, it is reasonable to consider that the maximum impact energy of each collision attainable with 3 mm balls represents the upper limit of solely physical grinding. Therefore, we empirically define $e_{crit} = 1.1 \times 10^{-3}$ J per hit as the maximum impact energy of each collision observed in simulations using 3 mm balls (Fig. S1, ESI†), beyond which solid-state chemical reaction is likely to occur. This definition helps to quantify the impact energy contributed to sub-critical collisions (physical grinding process) and supra-critical collisions (solid-state chemical reaction process) during ball milling. Accordingly, the cumulative impact energy E can be divided into two domains based on e_{crit}, as shown in Fig. 2b and c and calculated using the following equations:

$$E_{sub} = \int_0^{e_{crit}} e \times n(e)\mathrm{d}e \quad (5)$$

$$E_{supra} = \int_{e_{crit}}^{e_{max}} e \times n(e)\mathrm{d}e \quad (6)$$

Here, E_{sub} denotes the cumulative sub-critical impact energy, which contributes mainly to physical grinding, while E_{supra} denotes the cumulative supra-critical impact energy, associated with the chemical reaction.

As for the solid-state chemical conversion of $(HSiO_{1.5})_n$ to crystalline Si embedded in the SiO_2 matrix, the mechanism has

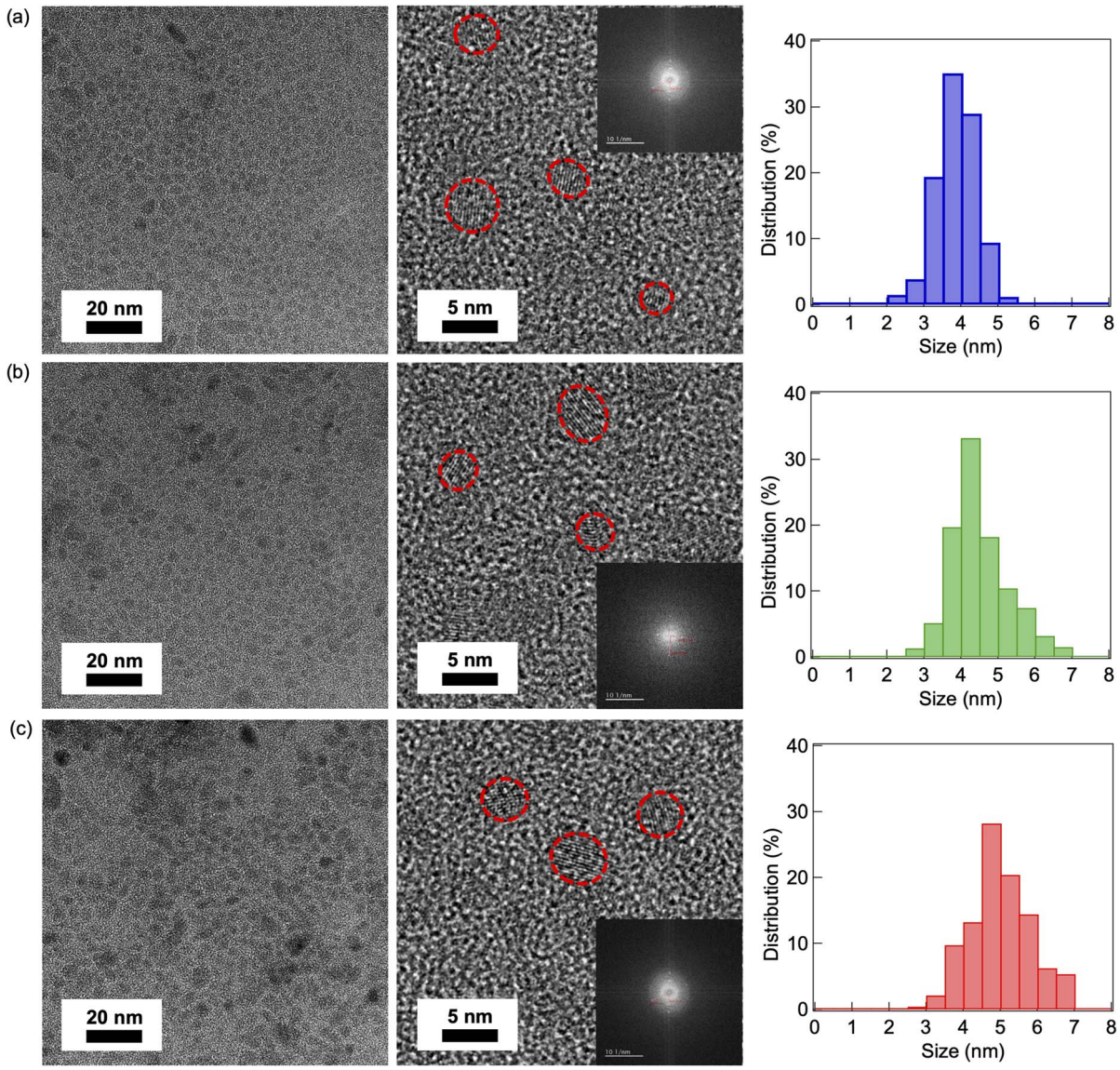

Fig. 5 HR-TEM images observed under altered magnification and estimated size distributions of (a) B-, (b) G-, and (c) R-Si QDs.

been clarified as follows: the cleavage of the Si–H bond in the $(HSiO_{1.5})_n$ molecule facilitates the generation of Si radicals and the resulting formation of H_2 and nanocrystalline Si, while the remaining Si–O–Si network transforms into a SiO_2-like matrix through the collapse of the raw $(HSiO_{1.5})_n$ structure and bond redistribution during the mechanochemical process.[28] The generation of Si radicals can be confirmed by ESR spectroscopy as displayed in Fig. 3a, where the signal can be attributed to the E' centre, with a structure of $^{\bullet}Si{\equiv}O$.[33–35] Further quantification of the ESR peak intensity as a function of E_{supra} during milling A1–A4 is summarized in Fig. 3b. The generation of H_2 leads to an increased pressure in the milling vessel. The pressure and temperature are directly monitored using an EASY GTM system equipped in the vessel (Fig. 3c), and the amount of H_2 produced is calculated according to the ideal gas law. The chemical structure cleavage of the $(HSiO_{1.5})_n$ molecule can be quantified by the reduction of Si–H (calculated from FT/IR) as well as the amount of generated H_2, as illustrated in Fig. 3d. Notably, these results demonstrate good correlation between the chemical conversion of the $(HSiO_{1.5})_n$ polymer (including the formation of Si radicals and H_2 and Si–H bond cleavage) and the E_{sup}. Therefore, we propose that under high-energy milling conditions using larger balls, a significant portion of collisions surpass e_{crit}, leading to an efficient solid-state chemical reaction. The preferential contribution of the larger E_{supra} aligns with the observed crystalline evolution, as it provides sufficient localized energy to overcome activation barriers for both bond dissociation and structural reorganization, thereby synergistically promoting QD growth and crystallinity enhancement. The observed chemical conversion scales with E_{supra}, underscoring its important role in driving mechanochemical reactions.

After mechanochemical treatment, the free-standing surface passivated alkyl-Si QDs were liberated from the SiO_2 matrix by chemical etching, followed by thermal hydrosilylation of selected mechanochemically treated $(HSiO_{1.5})_n$ polymers of A1, A3, and A4. The PL spectra of each alkyl-Si QD recorded by changing the excitation wavelength are shown in Fig. 4a–c. The alkyl-Si QDs obtained in A1, where only 5 mm mill balls were used for mechanochemical treatment, exhibit visible PL ranging from 400 to 600 nm wavelengths with the strongest emission at 450 nm as illustrated in Fig. 4a. Meanwhile, the PL peak of the alkyl-Si QDs obtained in A3 ranges from 400 to 600 nm wavelengths shows the strongest emission at 520 nm located in the green light region, as observed in Fig. 4b. When only larger balls were used in mechanochemical treatment as in A4, excitation-independent emission peaks with a strong emission peak at 620 nm were observed for alkyl-Si QDs (Fig. 4c). As shown by the photograph in Fig. 3d, bright blue, green, and red emissions are observed under 375 nm UV excitation for alkyl-Si QDs obtained from A1, A3, and A4, respectively, which are hereafter referred to as B-, G-, and R-Si QDs. The main PL peaks of B- and G-Si QDs, located in blue and green spectral regions, are red shifted with increasing excitation wavelength. This shift has been ascribed to the size distribution

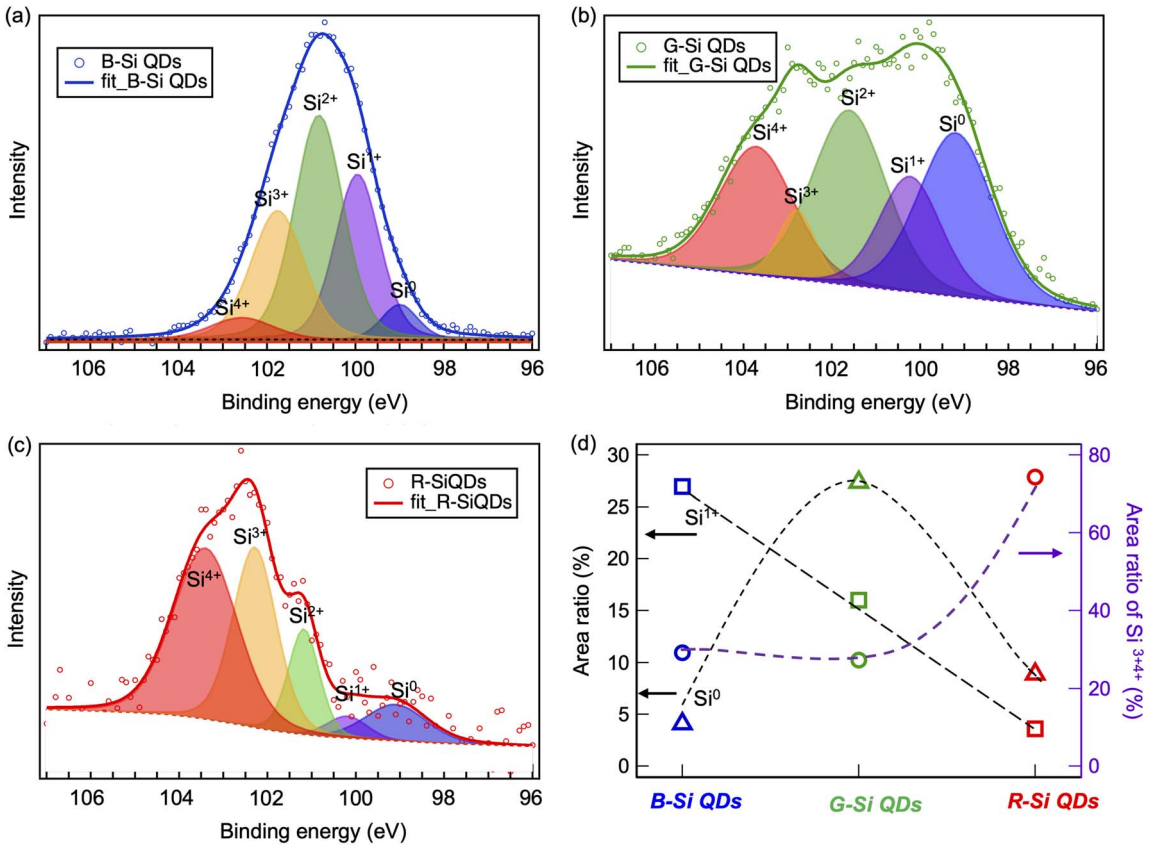

Fig. 6 XPS profiles of the Si 2p orbital of (a) B-, (b) G-, and (c) R-Si QDs. (d) Calculated peak area of different Si states.

of the Si QDs, whereby excitation at longer wavelengths produces excited states for larger Si QDs due to the quantum confinement effect.[8,36–39] In contrast, the PL peaks of the R-Si QDs and the minor shoulder in B- and G-Si QDs are independent of the excitation wavelength, suggesting that the emissions originate from surface or interface-related trap states.[8,37,40] The wavelength-tunable Si QDs synthesized *via* the green and sustainable mechanochemical route from the $(HSiO_{1.5})_n$ polymer exhibit significant PL properties and the QYs of B-, G-, and R-Si QDs were evaluated to be 4.5%, 5.3%, and 9.5%, respectively.

The HR-TEM observation was conducted to confirm the morphology and crystallinity of the synthesized alkyl-Si QDs. Fig. 5a–c show the HR-TEM images of B-, G-, and R-Si QDs, showing that they were well dispersed with a spherical shape. The related FFT patterns (inset figures) of the selected particle reveal the presence of the (111) and (220) crystallographic planes of crystalline Si, whose interplanar spacings are 0.31 and 0.19 nm, respectively, which clearly demonstrate the formation of Si QDs.[41] Regarding the results of size distribution as estimated from HR-TEM images, the core size of the synthesized Si QDs increases as the ratio of larger balls used in the mechanochemical treatment process increases. The sizes of the B-, G-, and R-Si QDs are estimated to be 3.60, 4.23, and 4.74 nm, respectively, which are smaller than the hydrodynamic size measured in toluene solution as analysed in DLS measurement (Fig. S2, ESI†). These results demonstrate that the size of the synthesized Si QDs in the mechanochemical process can be well controlled by adjusting the size of the milling balls, or the ratio of large to small milling balls, as the size increase is primarily governed by the prevalence of E_{supra} induced by the larger milling balls.

In general, the red shift is observed in the PL as the size of Si QDs increases, due to the recombination of electrons and holes based on quantum confined band structure in the core state.[36–39] Besides the size-dependent emission, the surface state of Si QDs may also play an important role in these wavelength-tunable Si QDs.[8,36] Therefore, the chemical states and functional forms present in the synthesized samples are investigated by XPS. Fig. 6a–c show the high-resolution XPS scans of the Si 2p orbital for B-, G-, and R-Si QDs, respectively. The spectra are analyzed by peak fitting into five peaks at 99.3, 100.3, 101.9, 102.9 and 104.1 eV, corresponding to Si^0, Si^+, Si^{2+}, Si^{3+} and Si^{4+} states, respectively.[42] It indicates the presence of Si–Si core comprising low-valent state Si passivated by alkyl-chains, along with high-covalent oxidated Si (Si^{3+}, Si^{4+}) on surface. As shown in Fig. 6d, the proportion of high-valent Si increases significantly from B-/G- to R-Si QDs, suggesting that larger QDs are more susceptible to oxidation during or after the synthesis. Moreover, the number of carbon chains on the Si QD surfaces was also quantified based on a previously reported procedure.[43,44] As a result, the coverage of carbon chains on the synthesized B-, G-, and R-Si QDs was estimated to be 72%, 69%, and 54%, respectively.

To verify the origin of PL, the PL lifetime was analysed to investigate the radiative and non-radiative dynamics of Si QDs. As shown in Fig. 7a, the time decay of PL plotted by small open

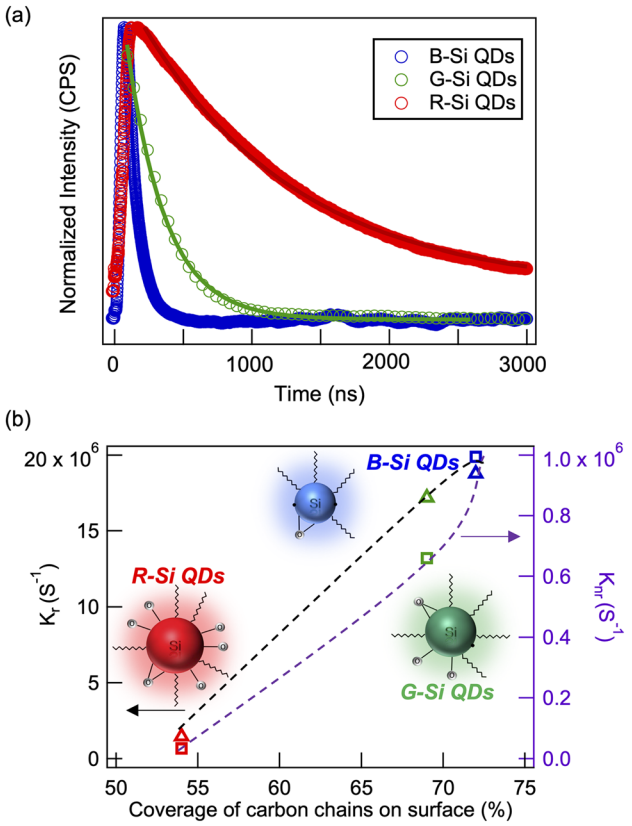

Fig. 7 (a) PL decay curve of B-, G-, and R-Si QDs. (b) Radiative (left axis) and non-radiative (right axis) recombination rates as a function of surface coverage of alkyl chains of R-, G-, and B-Si QDs. (Inset illustrations represent the proposed R-, G-, and B-Si QDs; balls at the centre: Si core; white balls: oxygen; polylines: alkyl chains on the surface.)

circles can be satisfactorily fitted to the theoretical curve of the exponential function with the time constant. Based on the calculations,[44–46] the lifetimes of B-, G-, and R-Si QDs are estimated to be 47.9 ns, 71.1 ns, and 1.35 μs, respectively. The observed fast blue-green PL was reported to arise from the band-to-band recombination of electrons and holes confined in the Si QD core, with the carriers trapped at O-related defect states at the surface of the Si QDs giving rise to microsecond decaying red PL.[36] The calculated values of the radiative recombination rate (K_r) and non-radiative recombination (K_{nr}) as a function of surface carbon chain coverage of each Si QD are illustrated in Fig. 7b. The values of K_r near 10^7 s^{-1} are in good agreement with those for the blue and green PL from carbon chain-capped Si QDs.[36] It has been well known that the alkyl chains on the Si QD surface can enhance the radiative transitions by modification of the electron and hole wavefunctions as a direct band gap-like character,[22,36] which exactly explains the increasing radiative recombination rate as the surface alkyl chain coverage increases for R-, G, and B-Si QDs. Si dangling bonds act as trapping centres, and the surface passivation of dangling bonds results in a reduction of non-radiative pathways.[42,47–50] The QY enhancement was previously observed for Si QDs aged in water and was attributed to reduced non-radiative recombination by

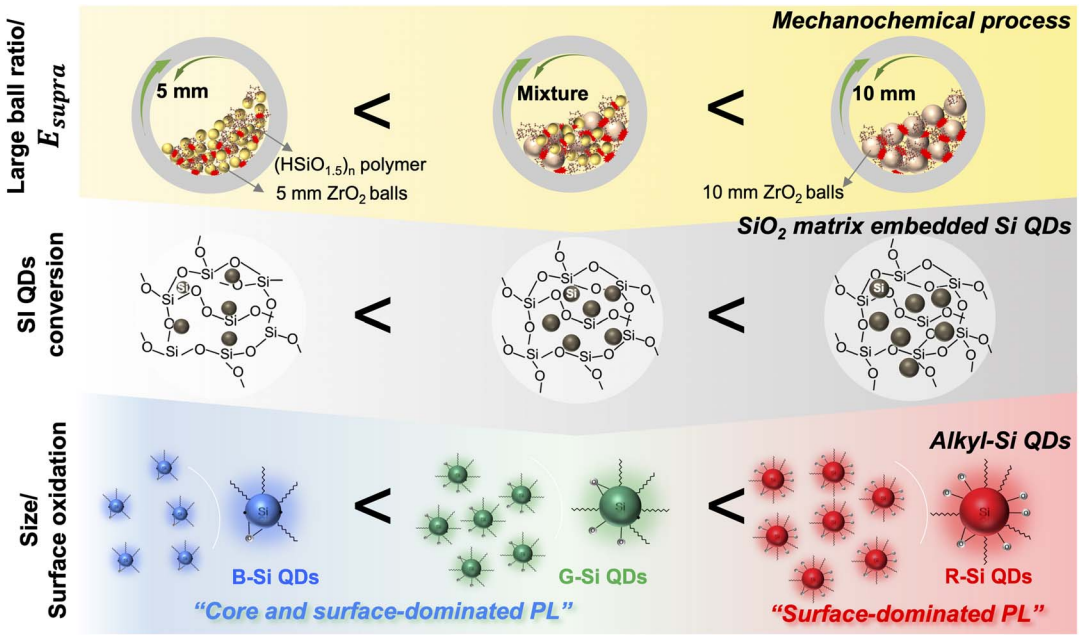

Scheme 2 Schematic illustration of the mechanochemical assembly process leading to wavelength-tunable photoluminescent alkyl-functionalized Si QDs.

passivation of dangling bonds due to oxygen during aging.[51] Therefore, for R-Si QDs, more heavy surface oxidation is also beneficial for less non-radiative recombination. Overall, we propose a dual-mechanism origin of the PL in the synthesized alkyl-Si QDs. For B- and G-Si QDs, the emission is dominated by two possibilities corresponding to both core and surface state recombination of excited electrons and holes, facilitated by sufficient alkyl passivation that suppresses non-radiative decay. For R-Si QDs, emission arises primarily from surface-localized oxide states, formed due to reduced organic coverage and heavy oxidation, resulting in excitation-independent PL and longer lifetimes.

Therefore, the PL evolution from blue to red in these sustainably synthesized alkyl-functionalized Si QDs is governed by a size–surface coupling effect inherently linked to the mechanochemical assembly process (as illustrated in Scheme 2). The conversion of Si QDs from the $(HSiO_{1.5})_n$ polymer, manifested by the increase in the size and crystallinity of Si QDs, is primarily dictated by E_{supra}, which is tunably modulated through the selection of larger milling balls. Under identical chemical etching and passivation conditions, the larger QDs exhibit more extensive surface oxidation, resulting in a transition of the PL mechanism from mixed core and surface contributions to predominantly surface-dominated emission. This tunable PL evolution underscores the critical role of the green mechanochemical strategy in tailoring both the structure and emission properties of functional Si QDs.

Conclusions

In this study, we present a sustainable and environmentally friendly approach to synthesize functional Si QDs exhibiting tunable PL within the visible light spectrum. Importantly, Si QDs synthesized through a room-temperature mechanochemical route using a $(HSiO_{1.5})_n$ polymer as the precursor allow for precise control over both the size and surface chemical characteristics of the functional Si QDs through mechanochemical treatment, followed by hydrosilylation. With systematic elucidation of the crystalline size and surface chemical state of the synthesized Si QDs, a clear correlation between their optical properties and relative size/surface chemical state is established. Combined with simulated ball motion by DEM during milling, our mechanistic analysis reveals that the formation of Si radicals and cleavage of Si–H bonds exhibit a strong dependence on the cumulative supra-critical impact energy E_{supra}, the total energy from collisions that exceed the reaction threshold (e_{crit}). This finding suggests that high-energy collisions, particularly those generated by larger milling balls, play a critical role in overcoming activation barriers for chemical structure conversion of $(HSiO_{1.5})_n$ molecules, thereby facilitating the solid-state transformation and the growth of crystalline Si. Thus, we conclude that the size increase of Si QDs in the mechanochemical process is primarily governed by the prevalence of E_{supra} induced by the larger milling balls. Building upon this mechanistic understanding of size evolution during the mechanochemical process, we further clarify the origin of PL in the synthesized alkyl-Si QDs. The observed evolution in emission energy across B-, G-, and R-Si QDs cannot be solely explained by quantum confinement effects. Instead, the PL characteristics result from a coupled influence of size-dependent surface chemistry. As the Si QD size decreases, a higher density of surface alkyl chains is observed, which effectively enhances both core and surface state recombination of excited electrons and holes. Conversely, larger Si QDs exhibit

more extensive surface oxidation due to their increased surface area and reduced alkyl coverage. Therefore, the gradual red shift in PL and the change in the emission mechanism reflect an intrinsic size–surface correlation: with increasing size, the dominant contribution to PL shifts from quantum-confined core and surface states to oxygen-related surface states. These findings not only underscore the viability of a green and sustainable synthesis route for functional Si QDs but also provide valuable insights into the factors governing their optical properties. This research paves the way for the development of Si QDs with tailored optical characteristics, holding promise for applications ranging from optoelectronics to bioimaging and beyond. The present strategy offers a scalable and environmentally conscious pathway toward next-generation optoelectronic nanomaterials.

Data availability

The data supporting this article have been included as part of the ESI.†

Conflicts of interest

There are no conflicts to declare.

Acknowledgements

The author acknowledges Prof. Dr Toru Asaka (Nagoya Institute of Technology) for HR-TEM observations. The author acknowledges the development of KIK DEM (Ver1.4) simulation software, which was supported by the Institute of Multidisciplinary Research for Advanced Materials (IMRAM) of Tohoku University, Joining and Welding Research Institute (JWRI) of Osaka University, and National Institute for Materials Science (NIMS, Japan).

References

1 D. V. Talapin, J.-S. Lee, M. V. Kovalenko and E. V. Shevchenko, *Chem. Rev.*, 2010, **110**, 389–458.
2 C. de Mello Donegá, *Chem. Soc. Rev.*, 2011, **40**, 1512–1546.
3 L. Pavesi and R. Turan, *Silicon Nanocrystals: Fundamentals, Synthesis and Applications*, John Wiley & Sons, 2010.
4 X. Liu, Y. Zhang, T. Yu, X. Qiao, R. Gresback, X. Pi and D. Yang, *Part. Part. Syst. Charact.*, 2016, **33**, 44–52.
5 B. Gelloz, F. B. Juangs, T. Nozaki, A. Koji, N. Koshid and L. Jin, *Front. Phys.*, 2019, **7**, 47.
6 I. Sychugov, F. Pevere, J. W. Luo, A. Zunger and J. Linnros, *Phys. Rev. B*, 2016, **93**, 161413.
7 A. P. Alivisatos, *J. Phys. Chem.*, 1996, **100**, 13226–13239.
8 K. Dohnalová, T. Gregorkiewicz and K. Kůsová, *J. Phys.: Condens. Matter*, 2014, **26**, 173201.
9 M. Dasog, G. B. De los Reyes, L. V. Titova, F. A. Hegmann and J. G. C. Veinot, *ACS Nano*, 2014, **8**, 9636–9648.
10 Y. Xu, Y. Xin and T. Shirai, *Annual Report*, Advanced Ceramics Research Center, Nagoya Institute of Technology, 2022, vol. 11, pp. 13–26.
11 A. Gupta, C. Schulz and H. Wiggers, *J. Optoelectron. Adv. Mater.*, 2010, **12**, 518.
12 F. Hua, M. T. Swihart and E. Ruckenstein, *Langmuir*, 2005, **21**, 6054–6062.
13 S. Sato and M. T. Swihart, *Chem. Mater.*, 2006, **18**, 4083–4088.
14 X. D. Pi, R. W. Liptak, J. D. Nowak, N. P. Wells, C. B. Carter, S. A. Campbell and U. Kortshagen, *Nanotechnology*, 2008, **19**, 245603.
15 Z. Kang, Y. Liu, C. H. A. Tsang, D. D. D. Ma, X. Fan, N. B. Wong and S. T. Lee, *Adv. Mater.*, 2009, **21**, 661–664.
16 L. Mangolini, E. Thimsen and U. Kortshagen, *Nano Lett.*, 2005, **5**, 655–659.
17 J. D. Holmes, K. J. Ziegler, R. C. Doty, L. E. Pell, K. P. Johnston and B. A. Korgel, *J. Am. Chem. Soc.*, 2001, **123**, 3743–3748.
18 P. Das, A. Saha, A. R. Maity, S. C. Ray and N. R. Jana, *Nanoscale*, 2013, **5**, 5732.
19 C. M. Hessel, E. J. Henderson and J. G. C. Veinot, *Chem. Mater.*, 2006, **18**, 6139–6146.
20 M. Dasog, K. Bader and J. G. C. Veinot, *Chem. Mater.*, 2015, **27**(4), 1153–1156.
21 E. J. Henderson, J. A. Kelly and J. G. C. Veinot, *Chem. Mater.*, 2009, **21**, 5426–5434.
22 Y. Xin, R. Wakimoto and K. I. Saitow, *Chem. Lett.*, 2017, **46**, 699–702.
23 S. Terada, Y. Xin and K. I. Saitow, *Chem. Mater.*, 2020, **32**, 8382–8392.
24 R. J. Clark, M. Aghajamali, C. M. Gonzalez, L. Hadadi, M. A. Islam, M. Javadi, M. H. Mobarok, T. K. Purkait, C. J. T. Robidillo, R. Sinelnikov, A. N. Thiessen, J. Washington, H. Yu and J. G. C. Veinot, *Chem. Mater.*, 2017, **29**, 80–89.
25 Y. Yu, G. Fan, A. Fermi, R. Mazzaro, V. Morandi, P. Ceroni and B. A. Korgel, *J. Phys. Chem. C*, 2017, **121**, 23240–23248.
26 I. Sychugov, A. Fucikova, F. Pevere, Z. Yang, J. G. C. Veinot and J. Linnros, *ACS Photonics*, 2014, **1**, 998–1005.
27 T. Ono, Y. Xu, T. Sakata and K. I. Saitow, *ACS Appl. Mater. Interfaces*, 2022, **14**, 1373–1388.
28 Y. Xu, Y. Xin, K. Kato and T. Shirai, *J. Mater. Chem. C*, 2022, **10**, 12588.
29 C. M. Hessel, E. J. Henderson and J. G. C. Veinot, *J. Phys. Chem. C*, 2007, **111**, 6956–6961.
30 J. Kano, H. Mio, F. Saito and M. Miyazaki, *Miner. Eng.*, 2001, **14**, 1213–1223.
31 R. Watanabe, K. Kushimoto, S. Ishihara and J. Kano, *J. Soc. Powder Technol., Jpn.*, 2019, **56**, 218–225.
32 N. Muanpaopong, R. Davé and E. Bilgili, *Powder Technol.*, 2023, **421**, 118454.
33 A. Stesmans and V. V. Afanas'ev, *Appl. Phys. Lett.*, 1996, **69**, 2056–2058.
34 A. Stesmans, *J. Non-Cryst. Solids*, 1994, **179**, 10–21.
35 D. L. Griscom, *Phys. Rev. B: Condens. Matter Mater. Phys.*, 1980, **22**, 4192.
36 K. Dohnalová, A. N. Poddubny, A. A. Prokofiev, W. D. A. M. de Boer, C. P. Umesh, J. M. J. Paulusse, H. Zuihof and T. Gre, *Light: Sci. Appl.*, 2013, **2**, 47.

37 M. J. L. Portolles, R. P. Diez, M. L. Dell'Arciprete, P. Caregnao, J. J. Romero, D. O. Martire, O. Azzaroni, M. Ceolin and M. C. Gonzalez, *J. Phys. Chem. C*, 2012, **116**, 11315.
38 J. Valenta, A. Fucikova, I. Pelant, K. Dohnalova, A. Aleknavicius, O. Cibulka, A. Fojtik and G. Kada, *New J. Phys.*, 2008, **10**, 073022.
39 K. Dohnalová, A. Fucikova, C. P. Umesh, J. Humpolickova, J. M. Paulusse, J. Valenta, H. Zuihof, M. Hof and T. Gregorkiewicz, *Small*, 2012, **8**, 3185.
40 S. Yang, W. Li, B. Cao, H. Zeng and W. Cai, *J. Phys. Chem. C*, 2011, **115**, 21062.
41 N. Saxena, A. Agarwal, D. M. Phase, R. J. Choudhary and D. Kanjilal, *Phys. E*, 2012, **42**, 2190.
42 Z. Yang, G. B. De los Reyes, L. V. Titova, I. Sychugov, M. Dasog, J. Linnros, F. A. Hegmann and J. G. C. Veinot, *ACS Photonics*, 2015, **2**, 595–605.
43 M. Rosso-Vasic and E. Spruijt, *Small*, 2008, **4**, 1835.
44 D. Tan, Z. Ma, B. Xu, Y. Dai, G. Ma, M. He, Z. Jin and J. Qiu, *Phys. Chem. Chem. Phys.*, 2011, **13**, 20255.
45 A. Sillen and Y. Engeborghs, *Photochem. Photobiol.*, 1998, **67**, 475.
46 M. L. Mastronardi, F. Maier-Flaig, D. Faulkner, E. J. Henderson, C. Kubel, U. Lemmer and G. A. Ozin, *Nano Lett.*, 2012, **12**, 337.
47 E. Cartier, J. H. Stathis and D. A. Buchanan, *Appl. Phys. Lett.*, 1993, **63**, 1510–1512.
48 C. Delerue, G. Allan and M. Lannoo, *Phys. Rev. B: Condens. Matter Mater. Phys.*, 1993, **48**, 11024.
49 S. Godefroo, M. Hayne, M. Jivanescu, A. Stesmans, M. Zacharias, O. I. Lebedev, G. Van Tendeloo and V. V. Moshchalkov, *Nat. Nanotechnol.*, 2008, **3**, 174.
50 K. Sato and K. Hirakuri, *J. Appl. Phys.*, 2006, **100**, 114303.
51 S. Yang, W. Cai, H. Zeng and Z. Li, *J. Appl. Phys.*, 2008, **104**, 023516.